Biomedical Optics EXPRESS

Feasibility of optical coherence elastography measurements of shear wave propagation in homogeneous tissue equivalent phantoms

Marjan Razani,[1,5] Adrian Mariampillai,[2] Cuiru Sun,[2] Timothy W. H. Luk,[1] Victor X. D. Yang,[1,2,3] and Michael C. Kolios[1,4]

[1]*Department of Physics, Ryerson University, Toronto, Canada*
[2]*Department of Electrical and Computer Engineering, Ryerson University, Toronto, Canada*
[3]*Division of Neurosurgery, University of Toronto, Toronto, Canada*
[4]*mkolios@ryerson.ca*
[5]*mrazani@ryerson.ca*

Abstract: In this work, we explored the potential of measuring shear wave propagation using optical coherence elastography (OCE) based on a swept-source optical coherence tomography (OCT) system. Shear waves were generated using a 20 MHz piezoelectric transducer (circular element 8.5 mm diameter) transmitting sine-wave bursts of 400 μs, synchronized with the OCT swept source wavelength sweep. The acoustic radiation force (ARF) was applied to two gelatin phantoms (differing in gelatin concentration by weight, 8% vs. 14%). Differential OCT phase maps, measured with and without the ARF, demonstrate microscopic displacement generated by shear wave propagation in these phantoms of different stiffness. We present preliminary results of OCT derived shear wave propagation velocity and modulus, and compare these results to rheometer measurements. The results demonstrate the feasibility of shear wave OCE (SW-OCE) for high-resolution microscopic homogeneous tissue mechanical property characterization.

OCIS codes: (170.4500) Optical coherence tomography; (170.6935) Tissue characterization.

References and links

1. J. Ophir, S. K. Alam, B. Garra, F. Kallel, E. Konofagou, T. Krouskop, and T. Varghese, "Elastography: ultrasonic estimation and imaging of the elastic properties of tissues," Proc. Inst. Mech. Eng. H **213**(3), 203–233 (1999).
2. C. Sun, B. Standish, and V. X. D. Yang, "Optical coherence elastography: current status and future applications," J. Biomed. Opt. **16**(4), 043001 (2011).
3. J. M. Schmitt, "OCT elastography: imaging microscopic deformation and strain of tissue," Opt. Express **3**(6), 199–211 (1998).
4. X. Liang, M. Orescanin, K. S. Toohey, M. F. Insana, and S. A. Boppart, "Acoustomotive optical coherence elastography for measuring material mechanical properties," Opt. Lett. **34**(19), 2894–2896 (2009).
5. J. F. Greenleaf, M. Fatemi, and M. Insana, "Selected methods for imaging elastic properties of biological tissues," Annu. Rev. Biomed. Eng. **5**(1), 57–78 (2003).
6. M. Fatemi and J. F. Greenleaf, "Application of radiation force in noncontact measurement of the elastic parameters," Ultrason. Imaging **21**(2), 147–154 (1999).
7. M. Elkateb Hachemi, S. Callé, and J. P. Remenieras, "Transient displacement induced in shear wave elastography: comparison between analytical results and ultrasound measurements," Ultrasonics **44**(Suppl 1), e221–e225 (2006).
8. L. Ostrovsky, A. Sutin, Y. Il'inskii, O. Rudenko, and A. Sarvazyan, "Radiation force and shear motions in inhomogeneous media," J. Acoust. Soc. Am. **121**(3), 1324–1331 (2007).
9. M. L. Palmeri, S. A. McAleavey, K. L. Fong, G. E. Trahey, and K. R. Nightingale, "Dynamic mechanical response of elastic spherical inclusions to impulsive acoustic radiation force excitation," IEEE Trans. Ultrason. Ferroelectr. Freq. Control **53**(11), 2065–2079 (2006).
10. W. F. Walker, F. J. Fernandez, and L. A. Negron, "A method of imaging viscoelastic parameters with acoustic radiation force," Phys. Med. Biol. **45**(6), 1437–1447 (2000).
11. K. Nightingale, M. S. Soo, R. Nightingale, and G. Trahey, "Acoustic radiation force impulse imaging: in vivo demonstration of clinical feasibility," Ultrasound Med. Biol. **28**(2), 227–235 (2002).

#163451 - $15.00 USD Received 27 Feb 2012; revised 8 Apr 2012; accepted 9 Apr 2012; published 16 Apr 2012

12. S. H. Yun, G. J. Tearney, J. F. de Boer, and B. E. Bouma, "Motion artifacts in optical coherence tomography with frequency-domain ranging," Opt. Express **12**(13), 2977–2998 (2004).
13. K. R. Nightingale, R. W. Nightingale, D. L. Stutz, and G. E. Trahey, "Acoustic radiation force impulse imaging of in vivo vastus medialis muscle under varying isometric load," Ultrason. Imaging **24**(2), 100–108 (2002).
14. M. Fatemi and J. F. Greenleaf, "Ultrasound-stimulated vibro-acoustic spectrography," Science **280**(5360), 82–85 (1998).
15. K. Nightingale, M. Palmeri, and G. Trahey, "Analysis of contrast in images generated with transient acoustic radiation force," Ultrasound Med. Biol. **32**(1), 61–72 (2006).
16. R. C. Chan, A. H. Chau, W. C. Karl, S. Nadkarni, A. S. Khalil, N. Iftimia, M. Shishkov, G. J. Tearney, M. R. Kaazempur-Mofrad, and B. E. Bouma, "OCT-based arterial elastography: robust estimation exploiting tissue biomechanics," Opt. Express **12**(19), 4558–4572 (2004).
17. S. J. Kirkpatrick, R. K. Wang, and D. D. Duncan, "OCT-based elastography for large and small deformations," Opt. Express **14**(24), 11585–11597 (2006).
18. S. G. Adie, X. Liang, B. F. Kennedy, R. John, D. D. Sampson, and S. A. Boppart, "Spectroscopic optical coherence elastography," Opt. Express **18**(25), 25519–25534 (2010).
19. X. Liang, S. G. Adie, R. John, and S. A. Boppart, "Dynamic spectral-domain optical coherence elastography for tissue characterization," Opt. Express **18**(13), 14183–14190 (2010).
20. B. F. Kennedy, X. Liang, S. G. Adie, D. K. Gerstmann, B. C. Quirk, S. A. Boppart, and D. D. Sampson, "In vivo three-dimensional optical coherence elastography," Opt. Express **19**(7), 6623–6634 (2011).
21. X. Liang and S. A. Boppart, "Biomechanical properties of in vivo human skin from dynamic optical coherence elastography," IEEE Trans. Biomed. Eng. **57**(4), 953–959 (2010).
22. B. F. Kennedy, T. R. Hillman, R. A. McLaughlin, B. C. Quirk, and D. D. Sampson, "*In vivo* dynamic optical coherence elastography using a ring actuator," Opt. Express **17**(24), 21762–21772 (2009).
23. A. Mariampillai, B. A. Standish, N. R. Munce, C. Randall, G. Liu, J. Y. Jiang, A. E. Cable, I. A. Vitkin, and V. X. Yang, "Doppler optical cardiogram gated 2D color flow imaging at 1000 fps and 4D in vivo visualization of embryonic heart at 45 fps on a swept source OCT system," Opt. Express **15**(4), 1627–1638 (2007).
24. J. Bercoff, M. Tanter, and M. Fink, "Supersonic shear imaging: a new technique for soft tissue elasticity mapping," IEEE Trans. Ultrason. Ferroelectr. Freq. Control **51**(4), 396–409 (2004).
25. K. Nightingale, S. McAleavey, and G. Trahey, "Shear-wave generation using acoustic radiation force: in vivo and ex vivo results," Ultrasound Med. Biol. **29**(12), 1715–1723 (2003).
26. J. McLaughlin and D. Renzi, "Using level set based inversion of arrival times to recover shear wave speed in transient elastography and supersonic imaging," Inverse Probl. **22**(2), 707–725 (2006).
27. M. L. Palmeri, S. A. McAleavey, G. E. Trahey, and K. R. Nightingale, "Ultrasonic tracking of acoustic radiation force-induced displacements in homogeneous media," IEEE Trans. Ultrason. Ferroelectr. Freq. Control **53**(7), 1300–1313 (2006).
28. G. F. Pinton and G. E. Trahey, "Continuous delay estimation with polynomial splines," IEEE Trans. Ultrason. Ferroelectr. Freq. Control **53**(11), 2026–2035 (2006).
29. J. McLaughlin and D. Renzi, "Shear wave speed recovery in transient elastography and supersonic imaging using propagating fronts," Inverse Probl. **22**(2), 681–706 (2006).
30. M. L. Palmeri, M. H. Wang, J. J. Dahl, K. D. Frinkley, and K. R. Nightingale, "Quantifying hepatic shear modulus in vivo using acoustic radiation force," Ultrasound Med. Biol. **34**(4), 546–558 (2008).
31. A. B. Karpiouk, S. R. Aglyamov, Y. A. Ilinskii, E. A. Zabolotskaya, and S. Y. Emelianov, "Assessment of shear modulus of tissue using ultrasound radiation force acting on a spherical acoustic inhomogeneity," IEEE Trans. Ultrason. Ferroelectr. Freq. Control **56**(11), 2380–2387 (2009).
32. A. P. Sarvazyan, O. V. Rudenko, S. D. Swanson, J. B. Fowlkes, and S. Y. Emelianov, "Shear wave elasticity imaging: a new ultrasonic technology of medical diagnostics," Ultrasound Med. Biol. **24**(9), 1419–1435 (1998).
33. M. Orescanin, "Complex shear modulus reconstruction using ultrasound," thesis (University of Illinois at Urbana-Champaign, 2010).
34. W. A. Berg, D. O. Cosgrove, C. J. Doré, F. K. W. Schäfer, W. E. Svensson, R. J. Hooley, R. Ohlinger, E. B. Mendelson, C. Balu-Maestro, M. Locatelli, C. Tourasse, B. C. Cavanaugh, V. Juhan, A. T. Stavros, A. Tardivon, J. Gay, J. P. Henry, and C. Cohen-Bacrie; BE1 Investigators, "Shear-wave elastography improves the specificity of breast US: the BE1 multinational study of 939 masses," Radiology **262**(2), 435–449 (2012).
35. M. Fatemi and J. F. Greenleaf, "Vibro-acoustography: an imaging modality based on ultrasound-stimulated acoustic emission," Proc. Natl. Acad. Sci. U.S.A. **96**(12), 6603–6608 (1999).
36. S. Chen, M. Fatemi, and J. F. Greenleaf, "Quantifying elasticity and viscosity from measurement of shear wave speed dispersion," J. Acoust. Soc. Am. **115**(6), 2781–2785 (2004).
37. K. R. Nightingale, R. Bentley, and G. E. Trahey, "Observations of tissue response to acoustic radiation force: opportunities for imaging," Ultrason. Imaging **24**(3), 129–138 (2002).
38. Y. Yamakoshi, J. Sato, and T. Sato, "Ultrasonic imaging of internal vibration of soft tissue under forced vibration," IEEE Trans. Ultrason. Ferroelectr. Freq. Control **37**(2), 45–53 (1990).
39. S. Chen, M. Fatemi, and J. F. Greenleaf, "Remote measurement of material properties from radiation force induced vibration of an embedded sphere," J. Acoust. Soc. Am. **112**(3), 884–889 (2002).
40. E. E. Konofagou and J. Ophir, "A new elastographic method for estimation and imaging of lateral displacements, lateral strains, corrected axial strains and Poisson's ratios in tissues," Ultrasound Med. Biol. **24**(8), 1183–1199 (1998).
41. C. Amador, M. W. Urban, S. Chen, Q. Chen, K.-N. An, and J. F. Greenleaf, "Shear elastic modulus estimation from indentation and SDUV on gelatin phantoms," IEEE Trans. Biomed. Eng. **58**(6), 1706–1714 (2011).

#163451 - $15.00 USD Received 27 Feb 2012; revised 8 Apr 2012; accepted 9 Apr 2012; published 16 Apr 2012

1. Introduction

Elastography is a method of generating stiffness and strain images of soft tissues for diagnostic purposes [1]. An imaging modality is used to detect tissue deformation behaviors under static or dynamic load and presents the resulting images as elastograms. Elastograms contain information about local variations of stiffness inside a region of interest, as well as additional clinical information such as the identification of suspicious lesions, the diagnosis of various disease states, and the monitoring of the effectiveness of treatments. Different imaging modalities such as ultrasound (US) imaging or magnetic resonance imaging (MRI) can be used to measure tissue displacements and estimate the resulting tissue mechanical properties [2]. Drawbacks of MRI include cost, long clinical wait times, and technological complexity. As well, both US and MRI have spatial resolutions in the order of 0.1-1 mm, which is insufficient for detecting small and subtle elastic variations in tissues, such as in small tumors and atherosclerotic plaques. Optical coherence tomography (OCT) is an optical tomographic imaging technique that shares many similarities to ultrasound imaging despite using light. OCT has several advantages over other imaging modalities, primarily due to its inherently high resolution, which allows for the identification of micron sized morphological tissue structures. Although the improved resolution comes at the expense of limited imaging penetration depth to the order of a few millimeters, OCT equipment is inexpensive and its interchangeable components enable experiment-specific flexibility. Optical coherence elastography (OCE) is a relatively new elastography technology that uses OCT to measure tissue displacement and biomechanical properties of soft tissues [3]. During OCE, tissues can be excited internally or externally, as well as statically or dynamically [4]. Methods for creating dynamic compressions include acoustic radiation force (ARF) and low-frequency vibrations with a needle [5].

ARF excitation for producing transient excitations has been implemented to assess the mechanical properties of tissues. ARF imaging is used in general elasticity imaging methods [6–10], for the characterization of lesions [11,12], muscle screening [13], and imaging of the calcification of arteries [14]. Most investigators are exploring methods to measure the tissue mechanical properties using external excitation of the tissue [15]. ARF has also been used for the internal mechanical excitation of a sphere embedded in a gelatin phantom, with phantom deformations detected with a spectral domain OCT (SD-OCT) system and recorded as M-mode phase images and then the displacement of the sphere over time was used for shear modulus measurements [4]. Tissue velocity and strain measurements have been obtained via tissue imaged under mechanical loading with a vascular OCE protocol specific to the exploring of tissue biomechanics [16]. Strain responses of tissue phantom undergoing compressive forces have been measured using speckle tracking and SD-OCT methods for detecting small and large deformations [17]. Spectroscopic OCE (S-OCE) has been utilized for frequency-dependent contrast of the displacement amplitude and phase of a silicone phantom, with ex vivo tumor follow-up imaging, in B-mode OCT imaging with applications in pathology [18]. As well, a dynamic SD-OCE technique applied to three-layer silicone tissue phantoms and ex vivo rat tumor tissue has been reported to provide contrast between sample regions with different mechanical properties, thus to mechanically characterize tissue [19]. In vivo three-dimensional OCE has also been implemented to observe elastic properties of superficial skin, which can be utilized for detecting strain rates and contrast useful for pathologists [20,21]. A ring actuator has also been applied to in vivo dynamic OCE to enable excitation and imaging for the same side of the sample, thus providing an alternative for contrast in OCT images [22].

We present a novel technique for calculating tissue mechanical properties by propagating shear waves in homogeneous tissue phantoms with ARF, and measuring the shear wave speed and its associated properties with OCT phase maps. The OCT phase maps are acquired with a swept-source OCT (SS-OCT) system. Although SS-OCT systems typically have higher phase

#163451 - $15.00 USD Received 27 Feb 2012; revised 8 Apr 2012; accepted 9 Apr 2012; published 16 Apr 2012

noise than SD-OCT systems, especially at high A-scan rates, the phase noise of the relatively low speed SS-OCT (8kHz bi-directional) used in these experiments was sufficient to measure phase changes induced by shear wave propagation [12,23]. The dynamic excitation OCE technique uses ARF as the excitation source. There are several ways that shear wave speed can be measured. These methods include the inversion of the Helmholtz Equation, which characterizes the shear wave propagation [24,25], using algorithms that measure lateral time for peak-to-peak displacements [26], tracking the displacement field jitters that are associated with shear waves [27,28], and using a variety of correlation-based algorithms [26,29]. The speed of shear waves that propagate in soft tissues is directly related to the shear modulus of the material [30,31]. Traditional compression wave imaging methodologies, such as US, provide measurements based on the tissue bulk modulus, which is confined to a relatively small range for soft tissues. The shear modulus for soft biological tissues actually span a much larger range compared to the bulk modulus by several orders of magnitude [32,33]. The use of the shear modulus as a cancer biomarker has been recently demonstrated using ultrasonic techniques [34]. In this work, shear modulus measurements of homogeneous tissue equivalent phantoms were made from OCT phase elastograms, without the requirement of measuring displacements of embedded targets. We present this methodology as Shear Wave OCE (SW-OCE). This method lays the foundation for future studies of mechanical property measurements of heterogeneous tissue structures, as well as potential research applications in pathology, intravascular studies, US/OCT needle probe imaging, and small animal studies.

2. Acoustic radiation force

Acoustic radiation force (ARF) is produced by a change in the energy density of the incident acoustic field [35,36]. The acoustic radiation force is generated by the transfer of momentum from the acoustic wave to the tissue. This force is applied in the direction of the longitudinal wave propagation and the magnitude of the force can be approximated by:

$$F = \frac{2\alpha I}{C}. \tag{1}$$

where F, kg/(s ^{2} cm ^{2}), is the acoustic radiation force, C (m/s) is the speed of sound in the medium, α (Np/m) is the absorption coefficient of the medium and I (W/cm^2) is the temporal

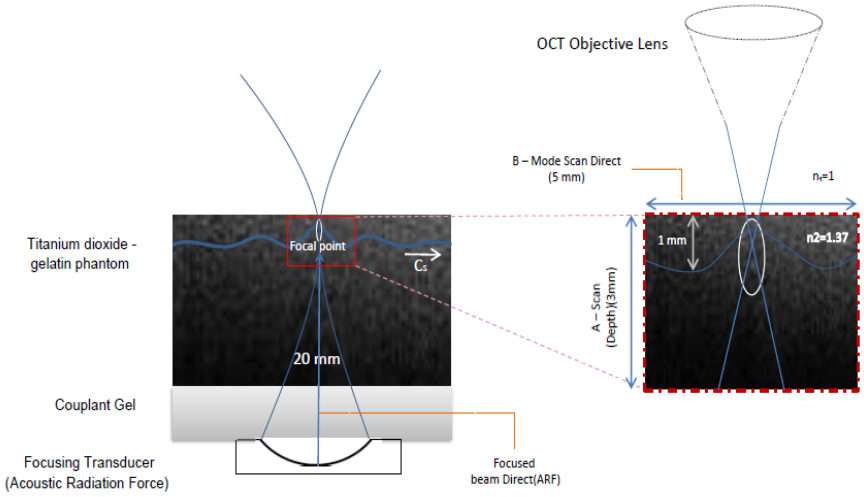

Fig. 1. Using a focused ARF impulse generated by a transducer, shear waves can be produced at the focal point. We detect the shear wave that travels within the titanium dioxide-gelatin phantom in the direction indicated by the white arrow labeled C_s. The transducer focal depth for this study was 20 mm. B-mode OCT images were taken at the focal point for phase map analysis.

#163451 - $15.00 USD Received 27 Feb 2012; revised 8 Apr 2012; accepted 9 Apr 2012; published 16 Apr 2012

average intensity at a given spatial location [37]. Figure 1 shows the principle of shear wave generation. Shear waves can be generated by using a focused impulse generated by an ultrasound transducer. The impulse creates a displacement in the direction of ultrasonic beam propagation which is largest at the transducer focus. After the impulse the material relaxes back to its original state producing a shear wave. The shear wave propagates in the direction perpendicular to the direction of the focused US propagation.

2.1 Shear moduli and wave propagation

By using the Voigt model for a homogenous medium, the shear wave speed C_s can be related to the shear modulus μ_1, shear viscosity μ_2, shear wave angular frequency ω, and tissue density ρ as follows [36,38,39]:

$$C_S(\omega) = \sqrt{2(\mu_1^2 + \omega^2\mu_2^2) / \rho(\mu_1 + \sqrt{\mu_1^2 + \omega^2\mu_2^2})}. \quad (2)$$

Experimentally, the displacements of shear waves at each tracking location are calculated with a speckle-tracking algorithm based on the OCT phase maps generated. The shear wave speed could be calculated using $\Delta\varphi$ and Δr measurements obtained from the measured phase shift, and the distance between the two tracking locations, respectively. The shear wave speed can be calculated using the following equation:

$$C_S(\omega) = \frac{\omega\Delta r}{\Delta\varphi}. \quad (3)$$

where $\omega = 2f$, $\Delta\varphi$ is the phase shift, and Δr *is* the distance between the two tracking locations. The shear wave frequency (f) is dependent on several factors, the most dominant of which is the beam width of the excitation transducer.

The Young's modulus and shear modulus are also important to defining the tissue mechanical properties. They can be calculated using the following equation (which assumes an isotropic homogeneous medium):

$$C_s = \sqrt{\frac{\mu}{\rho}} \quad (4)$$

and

$$E = 2(1+\nu)\mu \approx 3\mu = 3C_S{}^2\rho, \quad (5)$$

where ν, μ, and E represent the Poisson's ratio, shear modulus, and Young's modulus, respectively. Here we make the assumption that soft tissues are close to incompressible, with a constant Poisson's ratio of close to 0.5 (0.495) [40].

3. Materials and methods

In this study, we present a dynamic excitation OCE technique using ultrasound ARF as the excitation source. A custom SS-OCT system was used in this study. The laser had a center wavelength of a 1310 nm, a bandwidth of ~110 nm, and an A-scan rate of 8 kHz. The lateral resolution was approximately 13 μm in the samples. ARF (internal mechanical excitation) was applied using a 20 MHz, circular, 8.5 mm diameter piezoelectric transducer element (PZT, f-number 2.35) transmitting sine-wave bursts of 400 μs. The OCT images were taken with an existing swept-source system. B-mode images were taken of a titanium dioxide-gelatin phantom that was 5 mm in length. The OCT image A-scan depth was 3 mm. The focal point of the transducer used for the ARF experiments was 20 mm from the transducer surface and the focal spot was located about 1 mm below the top surface of the gelatin phantom. Figure 1 shows that M-mode images were taken along the y-direction, the direction of the ARF beam. Shear waves predominantly propagate radially outwards from the focal point, perpendicular to

#163451 - $15.00 USD Received 27 Feb 2012; revised 8 Apr 2012; accepted 9 Apr 2012; published 16 Apr 2012

the direction of the ARF beam (the shear waves propagate along the x-axis). The PZT element push sequence was synchronized with the OCT imaging triggering system. The US depth of field was 2.94 mm, with US focus of 20 mm. The full width at half maximum was calculated to be 246 μm.

The phantom in this study consisted of gelatin mixed with titanium dioxide, which provided uniform acoustic and optical scattering. Gelatin powder (Type B, Fisher Scientific, G7-500) and distilled water were heated in a water bath at 60–65°C for one hour and periodically stirred. Two tissue phantoms with different gelatin concentrations were prepared (Phantom 1: 14%, Phantom 2: 8%). When the phantom samples cooled to 45°C, 0.1% weight by weight titanium dioxide (Sigma-Aldrich, Titanium(IV) oxide nanopowder, <25 nm particle size, 99.7% trace metals basis) was added and thoroughly mixed. The phantom solution was poured into rectangle molds (20 mm height) and allowed to congeal. The titanium dioxide was used as a scattering agent. Figure 2 shows the schematic of the Acoustic Radiation Force-Optical Coherence Elastography (ARF-OCE) setup.

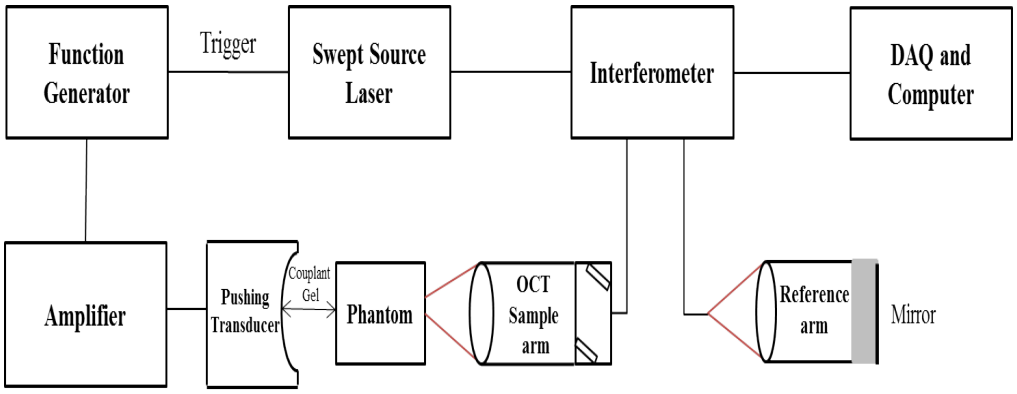

Fig. 2. The ARF-OCE experimental setup consisted of the existing SS-OCT system, a titanium dioxide-gelatin phantom, a focused transducer (20 MHz, f-number 2.35), an amplifier and a function generator (Agilent 33250A 80 MHz, Function / Arbitrary Waveform Generator) synchronized with the SS-OCT system.

The OCT signals from the phantoms were used for the measurement of the shear wave speed and mechanical properties. The US "push" transducer was synchronized with the OCT imaging system. The phase analysis was applied to B-mode and M-mode OCT images, which were obtained while the US transducer was generating the "push" in the phantom. A fast Fourier transform was performed on the OCT data, and phase maps of the phantom under US loading were generated and are directly related to the ARF induced displacement in the phantom.

Independent measurements of the mechanical properties of the phantom were made using a rheometer. Material properties of the same gelatin gels imaged using SW-OCE (14% w/w and 8% gelatin concentrations) were tested in a parallel-plate shear rheometer in oscillatory mode using a Physica MCR 301 rheometer (Anton Paar GmbH, Graz, Austria) equipped with Peltier plate temperature control unit (P-PTD 200). The parallel plate measuring geometry (PP 25/TG) with a diameter of 25mm was used. The frequency dependent elastic and viscous moduli, G' and G'', were measured for the 1 hour aged samples at 25°C for frequencies ranging from 10^{-1} Hz to10^{2} Hz. To avoid sample drying, the measuring geometry was covered with a solvent trap containing a moist strip of paper tissue. Preceding each measurement, the temperature of the Peltier plate was set at 10°C and the mixed hot biopolymer solution was poured directly onto the cold plate. The quenched sample rapidly transformed to a gel after which the temperature of the rheometer cell was raised from 10°C to 25°C at a rate of 6°C min^{-1}. The upper cone was then lowered onto the sample to an operating gap width (1 mm) and the sample was trimmed and held at 25°C for 10 minutes. Using this standard thermal treatment, the conventional gel state condition was readily satisfied for all samples. After

#163451 - $15.00 USD Received 27 Feb 2012; revised 8 Apr 2012; accepted 9 Apr 2012; published 16 Apr 2012

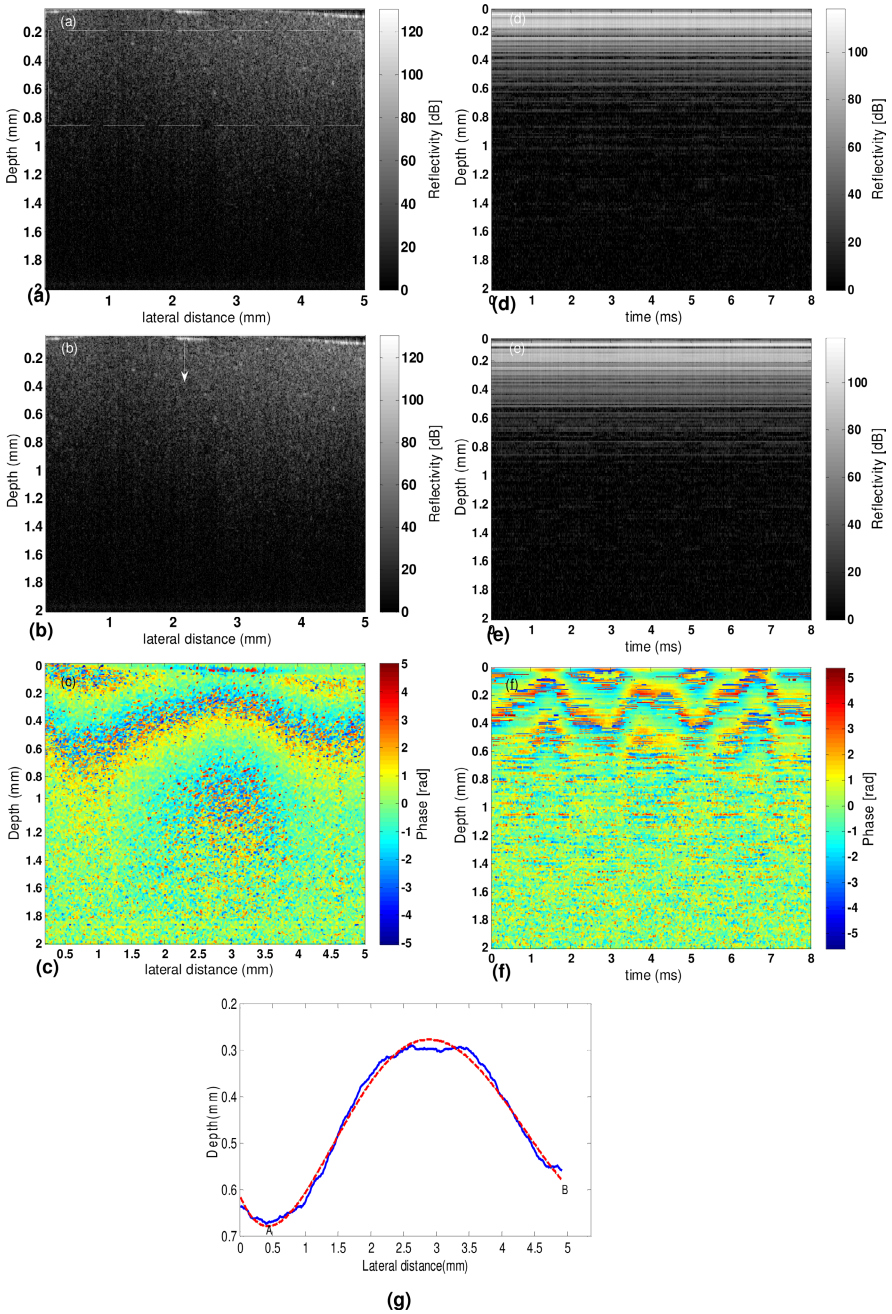

Fig. 3. B-mode OCT structural images (a and b) and the corresponding B-mode phase map (c) of the titanium dioxide-gelatin phantom (14%) were taken with the SS-OCT system. The dashed box(a) represents the location of the superimposed fitted sine wave observed in the phase map. The white arrow (b) indicates the position where the M-mode OCT images (d and e), with the ARF on and off, respectively, were acquired and synchronized with the OCT swept-source wavelength sweep. The B-mode phase map of the phantom was used to measure Δr and $\Delta\varphi$ for the calculation of the shear wave speed. The color scale represented the change of the phase value (radians). The M-mode phase map (f) from this phantom was used to calculate the shear wave frequency. To better illustrate the calculation of Δr, MATLAB was used to to plot an isophase curve which now shows the experimental data (blue). The red curve is a best fit with a polynomial (g).

#163451 - $15.00 USD Received 27 Feb 2012; revised 8 Apr 2012; accepted 9 Apr 2012; published 16 Apr 2012

thermal treatment, rheological measurements at 25°C were performed. To obtain the moduli at the dominant frequency of the shear waves generated in the SW-OCE experiments, the rheometer shear modulus versus frequency data had to be extrapolated to the value of interest.

4. Results and conclusion

OCT images of the titanium dioxide-gelatin phantom were taken with the SS-OCT system and shown in Fig. 3. B-mode and M-mode images of the phantom, as well as their respective phase maps provide information that is required to calculate distance, the phase shift between two locations and the shear wave frequency.

By measuring the time difference between successive troughs in the M-mode data set of Fig. 3(f), the dominant frequency of the shear wave was calculated to be approximately 266 Hz (for both the phantoms). The shear wave group speed was then calculated by using the Δr and $\Delta\varphi$ obtained from Figs. 3(c, g), which depicts the distance between the two successive locations and the measured phase shift, respectively. Two successive locations can be chosen at a particular depth z (in this work we chose z = 0.6 mm). At these two locations in the image, phase values are retrieved. The calculation of $\Delta\phi$ involves the measurements of the two phase values at the aforementioned two locations, which are then used in Eq. (3) to calculate the shear wave group velocity. Another way to illustrate a "snapshot" of the shear wave is to plot an isophase curve which was generated by averaging the phase value between depths from 0.25 mm to 0.7 mm Fig. 3(g). These values were then used in Eq. (3) to calculate the shear wave speed. The shear wave speeds for the 14% and 8% gelatin-titanium dioxide phantoms were 2.24 ± 0.06 m/s and 1.49 ± 0.05 m/s, respectively, and reported in Table. 1. The average values and standard deviations were calculated from 10 different pairs of locations in the phase maps for all calculations of Δr and $\Delta\varphi$.

The Young's moduli and shear moduli were also calculated using the above results. The measured density ρ of the phantom samples was 1050 kg/m^3. Table 1 summarizes the Young's moduli and shear moduli for both phantoms. The shear modulus estimated using SW-OCE for Phantom 1 (14%) was 5.3 ± 0.2 kPa and for Phantom 2 (8%) was 2.3 ± 0.1 kPa. The errors for the SW-OCE results represent the standard deviation. As expected, the values of the Young's moduli and shear moduli were greater for the phantom with the higher concentration of gelatin [41]. The shear moduli of both phantoms calculated using SW-OCE was compared to the shear moduli of the same two phantoms measured by the rheometer in Table 1. The errors for the rheometer results represent the standard deviations.

Table 1. The mechanical properties of the phantoms

Samples	Shear wave speed (C_s m/s)	Shear modulus (μ, kPa)	Young modulus (E, kPa)
Phantom 1 (14%)	2.24 ± 0.06	5.3 ± 0.2	15.8 ± 0.6
Rheometer		4.93 ± 0.05	
Phantom 2 (8%)	1.49 ± 0.05	2.3 ± 0.1	7.0 ± 0.3
Rheometer		2.06 ± 0.09	

In summary, we have demonstrated, for the first time, a SW-OCE technique that uses ARF for mechanical excitation of a homogeneous gelatin phantom to measure shear wave propagation. The mechanical excitation produces motions within the phantom that can be used for the estimation of mechanical properties using SW-OCE. This excitation produces shear waves that propagate perpendicular to the US beam. The close proximity of the transducer focus to the surface of the phantom suggests that the surface (Rayleigh) waves were produced [42]. The discrepancy between the values provided by the rheometer and the SW-OCE technique may be related to the extrapolation required from the rheometer data to obtain the values of the shear modulus at 266 Hz and the fact that the SW-OCE technique, as implemented, is more sensitive to the shear wave group velocity, whereas the shear modulus

#163451 - $15.00 USD Received 27 Feb 2012; revised 8 Apr 2012; accepted 9 Apr 2012; published 16 Apr 2012

from the rheometer is reported at one frequency. Possible *in vivo* clinical applications of this method of SW-OCE include pathology, intravascular studies, US/OCT catheter imaging, and small animal studies due to the potential for measuring mechanical properties within tissues as a disease assessments.

Acknowledgments

Marjan Razani is supported by an Ontario Graduate Scholarship (OGS). This work is funded in part by the Canada Research Chairs program (awarded to Drs. V.X.D. Yang and M. C. Kolios), the Natural Sciences and Engineering Research Council of Canada (NSERC discovery grant 216986-07) and Canada Foundation for Innovation. We would like to thank Dr. Mathias Fink, Dr. Hassan Firoozmand, Dr. Dérick Rousseau and Arthur Worthington for their contributions and discussions.

#163451 - $15.00 USD Received 27 Feb 2012; revised 8 Apr 2012; accepted 9 Apr 2012; published 16 Apr 2012